IOP Publishing Journal of Physics: Condensed Matter

J. Phys.: Condens. Matter **22** (2010) 055401 (8pp) doi:10.1088/0953-8984/22/5/055401

A gold–silicon potential fitted to the binary phase diagram

Seunghwa Ryu[1] **and Wei Cai**[2]

[1] Department of Physics, Stanford University, Stanford, CA 94305, USA
[2] Department of Mechanical Engineering, Stanford University, Stanford, CA 94305, USA

Received 6 October 2009, in final form 15 December 2009
Published 15 January 2010
Online at stacks.iop.org/JPhysCM/22/055401

Abstract

We develop an empirical interatomic potential model for the gold–silicon binary system that is fitted to the experimental phase diagram. The model is constructed on the basis of the modified embedded-atom-method formalism and its binary phase diagram is computed by efficient free energy methods. The eutectic temperature and eutectic composition of the model match well with the experimental values. We expect the model to be useful for atomistic simulations of gold-catalyzed growth of silicon nanowires.

(Some figures in this article are in colour only in the electronic version)

1. Introduction

The catalyzed growth of semiconductor nanowires (NWs) from gold nanoparticles via the vapor–liquid–solid (VLS) mechanism has been the subject of intensive research worldwide, due to their potential applications in nanotechnology [1, 2] and the opportunity to understand fundamental mechanisms of crystal growth at the nanoscale [3–5]. Si NW devices are especially desirable due to their potential compatibility with the existing silicon-based integrated circuit technology [6]. However, the integration of NW components into working devices requires a high degree of control that is still lacking, and many fundamental questions concerning NW nucleation and growth remain to be answered. The VLS mechanism of NW growth has been investigated using continuum theories of crystal growth [3, 7, 8]. While this approach succeeded in elucidating certain features of NW growth, it is still based on a phenomenological model. Fundamental kinetic relationships, such as the interface growth velocity as a function of the chemical potential difference, only appear as fitting parameters in the model. The question of how these kinetic relationship are affected by the small length scale of the NWs is beyond the scope of the continuum theories. The same can be said about the detailed mechanisms and the rate of NW nucleation, in which thermal fluctuation is expected to play an important role.

Atomistic simulations, such as molecular dynamics and Monte Carlo ones, should be able to probe the NW nucleation and growth processes in their full mechanistic detail. Currently, the progress in this direction has been hindered by two major challenges. First, we need an interatomic potential model that can accurately describe the interaction between gold and silicon atoms and remain computationally efficient. Second, we need advanced algorithms to extend the timescale of conventional simulation techniques (∼1 ns) to experimentally relevant timescales (∼1 s). In this paper, we address the first challenge by providing a new gold–silicon interatomic potential model that, for the first time, has been fitted to the binary phase diagram.

Because the number of atoms that are actively involved in the nucleation and growth of NWs easily exceeds a thousand, *ab initio* models become prohibitively expensive. Consequently, most of the atomistic simulations here would be based on empirical potential models, which can be fitted to *ab initio* or experimental data. While many empirical potential models already exist for pure gold and pure silicon, it is challenging to develop a model that describes the interaction between gold and silicon atoms. Being a face-centered-cubic (FCC) metal, gold can be well described by the embedded-atom-method (EAM) potentials [9], which contain a function that describes the energy required to embed an atom in the background electron density generated by its neighbors. Unfortunately, the EAM model does not work well for covalently bonded semiconductors such as silicon. Empirical models for silicon, such as the Stillinger–Weber [10] and Tersoff [11] ones, usually include terms that depend on the angles between two bonds for capturing the directionality and saturation of covalent bonds. Therefore, a gold–silicon model must be flexible enough to be able to describe both metallic and covalent bonds within the same framework.

A promising theoretical framework is the modified embedded-atom-method (MEAM), which extends EAM by

accounting for the angular distribution of background electron densities [12–14]. As a result, MEAM has been used to build models for many metals, semiconductors, and binary alloys [14–17]. The MEAM model for pure Si successfully describes the change of the coordination of Si atoms from fourfold to sixfold at melting [18], while the MEAM models for pure metals correctly capture the trend of surface energy [19, 20] and surface segregation [21, 22]. Therefore, in this work, we build the gold–silicon potential on the basis of the MEAM formalism. In order to be useful for NW growth studies, the potential needs to correctly capture the thermodynamic driving forces of crystallization. Hence we fit the potential to the experimental binary phase diagram, which is not done for most of the existing potential models in the literature. There have been previous studies on the development of EAM potentials consistent with the thermodynamics of the solid phases [23, 24]. The methods employed in these studies are not directly applicable to the fitting of the solid–liquid phase boundaries, which is the main focus of this paper.

There has been an earlier attempt to develop a MEAM gold–silicon potential [25, 26]. Unfortunately, we were unable to reproduce the published data. Hence we re-develop the MEAM potential here. Another attempt to construct a gold–silicon potential is to use EAM and Tersoff models to describe the interaction among gold atoms and silicon atoms, respectively, and to mix the two functional forms in an intuitive way to model gold–silicon interactions [27]. Because the phase diagrams for these two potential models have not been calculated, it is difficult to assess whether they are suitable for modeling the VLS growth of NWs. In preparation for this work, we have benchmarked the melting point and latent heat of the original MEAM potentials for pure gold and silicon, and adjusted the potentials to accurately reproduce the experimental values [28]. On the basis of these improved models, the remaining task amounts to constructing the cross-potential of gold and silicon. The fitting of the cross-potential to experimental phase diagrams is enabled by efficient free energy methods for rapidly calculating the phase diagram for a given candidate potential model.

The paper is organized as follows. In section 2, we present the functional form of our MEAM model for the gold–silicon system and the general procedure for determining its parameters. In section 3, we present our free energy methods used to compute the binary phase diagram from atomistic simulations. A brief summary is given in section 4. For completeness, we summarize the adjustments to the original MEAM potential for pure Au and pure Si [28] in appendix A. Appendix B contains a further benchmark of the Au–Si cross-potential, by comparing its predictions with *ab initio* data.

2. The MEAM model for gold and silicon

2.1. The functional form

The MEAM model describes the potential energy of a collection of atoms located at $\mathbf{r_i}$, $i = 1, \ldots, N$, using the following equation:

$$V(\{\mathbf{r_i}\}) = \sum_{i=1}^{N} F(\bar{\rho}_i) + \sum_{i=1}^{N-1} \sum_{j=i+1}^{N} S_{ij}\phi_{ij}(|\mathbf{r_i} - \mathbf{r_j}|) \quad (1)$$

where F is the embedding function, $\bar{\rho}_i$ is the background electron density at $\mathbf{r_i}$, S_{ij} is a multi-body screening factor and ϕ_{ij} is the pair potential of atoms i and j. The pair potential function $\phi_{ij}(r)$ is usually not given explicitly. Instead, it is defined as the function that, when combined with the embedding function, reproduces the universal equation of state (EOS) [31] for the chosen reference crystal structure. While the above functional form is similar to that of the embedded-atom-method (EAM), MEAM has two main extensions. First, the calculation of the background electron density $\overline{\rho_i}$ in MEAM accounts for the spatial arrangements of the neighboring atoms, in addition to their distance to atom i. Second, the range of the pair potential is cut off by a multi-body screening function S_{ij} that depends on the locations of atoms k that are neighbors of both atoms i and j. The details of the MEAM formalism are well described in the literature [14].

The pair potential function ϕ_{ij} depends on the species of the i–j atomic pair. The pair potential of two atoms of the same species is determined from the chosen EOS function for a reference crystal structure of that species. Here the reference structure for pure Si is a diamond-cubic (DC) crystal and that for pure gold is an FCC crystal. The EOS for these two reference structures have been adjusted to better fit the experimental melting temperature and latent heat of pure Si and Au [28]. To avoid ambiguity, we give a short summary on the improved MEAM potential for pure Au and pure Si [28] used in this work in appendix A.

For the Au–Si cross-potential, we choose the B1 structure as the reference structure. This is a hypothetical alloy structure because in the solid state the solubility of Au in Si (and vice versa) is very low. The EOS function used for the B1 crystal structure is

$$E^u(r) = -E_c\left(1 + a^* + \frac{\gamma}{r}\cdot a^{*3}\right)\exp(-a^*) \quad (2)$$

$$\text{with} \qquad a^* = \left(\frac{9\,\Omega B}{E_c}\right)^{1/2}\left(\frac{r}{r_e} - 1\right) \quad (3)$$

where r is the nearest-neighbor distance, E_c is the cohesive energy, r_e is the equilibrium nearest-neighbor distance, Ω is the atomic volume, and B is the bulk modulus of the reference structure. γ is an adjustable parameter present to provide additional flexibility [25].

2.2. Determining the parameters

We determine the parameters of the Au–Si cross-potential in three steps. First, we perform *ab initio* calculations of the hypothetical B1 alloy structure to determine the cohesive energy E_c, equilibrium nearest-neighbor distance r_e and bulk modulus B. Several MEAM parameters are determined by fitting to these values, after adjusting for the known differences between *ab initio* and experimental data. Second, the substitutional impurity energies of Si in FCC Au and Au in

Table 1. Equilibrium lattice constant a, bulk modulus B, cohesive energy E_c, and cubic elastic constants C_{11} and C_{44} for the DC structure of Si, FCC structure of Au, and B1 structure of Au–Si. For pure Si and Au, the differences between the experimental and *ab initio* values are listed in the column labeled 'offset'. Their average is the expected 'offset' value for the hypothetical B1 structure. The values marked with $*$ are the *ab initio* values plus the correction terms given in the 'offset' column. The last column is what the MEAM model is fitted to or predicts.

	Material	Experiment	DFT/LDA	Offset	MEAM
a (Å)	Si (DC)	5.431	5.390	−0.041	5.431
	Au (FCC)	4.070	4.068	−0.005	4.073
	Au–Si (B1)	5.184*	5.161	−0.023	5.400
B (GPa)	Si (DC)	98	96	2	98
	Au (FCC)	180	186	−6	180
	Au–Si (B1)	127*	129	−2	127
E_c (eV)	Si (DC)	4.63	5.976	−1.346	4.63
	Au (FCC)	3.93	4.387	−0.457	3.93
	Au–Si (B1)	4.155*	5.057	−0.902	4.155
C_{11} (GPa)	Si (DC)	164	162	2	164
	Au (FCC)	202	217	−15	202
	Au–Si (B1)	303*	310	−6	320
C_{44} (GPa)	Si (DC)	76	105	−29	76
	Au (FCC)	45	47	−2	45
	Au–Si (B1)	−35*	−19	−15	14

DC Si are computed *ab initio* and the data are used to adjust the electron density scaling factors ρ_0^{Au} and ρ_0^{Si}. Third, other potential parameters are adjusted from their default values so that the predicted binary phase diagram will reproduce the experimental diagram as accurately as possible. The parameters adjusted in the third step include γ in the EOS function of the alloy structure, and angular cut-off parameters $C_{min}(i, j, k)$ in the multi-body screening function S_{ij}. The first two steps are described in this section. The method used to compute the binary phase diagram is described in section 3.

Ab initio calculations are performed on the basis of the density functional theory (DFT) using VASP [29]. We employ the ultrasoft pseudopotentials [30] within the local density approximation, with plane-wave expansion up to a cut-off energy of 400 eV. A FCC (DC) unit cell consisting of four (eight) atoms is used for Au (Si). A B1 unit cell consisting of four Au atoms and four Si atoms is used for the solid alloy with B1 structure. For all cases, $15 \times 15 \times 15$ k-points are used with the Monkhorst–Pack scheme. The total energy was converged within 10^{-4} eV. The results for the DC crystal of Si, the FCC crystal of Au, and the hypothetical B1 structure of Au–Si are given in table 1.

Experimental data exist for crystals of pure Si and pure Au. The differences between experimental and *ab initio* data are listed in the column labeled 'offset'. This difference must be accounted for because existing MEAM models have been fitted to experiments instead of *ab initio* data. The correction to the *ab initio* data for the hypothetical B1 structure is obtained by averaging the differences between experimental and *ab initio* data for pure Si and Au. The data after this correction are marked with $*$ in table 1. These are the data that the MEAM model is fitted to, or should be compared against. We note that this adjustment of the VASP data is not unique and could lead to errors. The parameters r_e, E_c and $\alpha \equiv \sqrt{9\Omega B/E_c}$ in the EOS of the B1 reference structure are easily obtained with this approach. We note that we intentionally fit the lattice constant of the B1 structure to a larger value of $a = 5.400$ Å eV than the adjusted *ab initio* data (5.184 Å) (see appendix B), because it gives rise to better agreement with experiments for the binary phase diagram.

Table 2. MEAM and *ab initio* (DFT/LDA) predictions of impurity energies. E_1 is the energy needed to substitute an atom in an FCC Au crystal with a Si atom. E_2 is the energy needed to substitute an atom in a DC Si crystal with a Au atom.

	MEAM	DFT/LDA
E_1 (eV)	0.636	0.634
E_2 (eV)	3.968	1.553

The electron density scaling factors, ρ_0^{Au} and ρ_0^{Si}, do not affect the energy of pure crystals but influence the interaction between Au and Si atoms. Because only the ratio of the electron density scaling factors, $\frac{\rho_0^{Au}}{\rho_0^{Si}}$, is important, we have a single parameter to fit the two dilute solution energies. The ratio is adjusted to produce reasonable substitutional impurity energies, i.e. the energy E_1 for replacing a Au atom in the FCC crystal by a Si atom, and the energy E_2 for replacing a Si atom in the DC crystal by a Au atom. The MEAM and *ab initio* results for the impurity energies are listed in table 2. It shows that our choice of $\frac{\rho_0^{Au}}{\rho_0^{Si}}$ is the result of a compromise between E_1 and E_2, because we cannot fit both of them accurately. As a result, only E_1 is fitted while E_2 is overestimated. This disagreement of the MEAM result can be due to either the adjustment of VASP data introduced in table 1 or inaccuracies in the MEAM formalism. Nonetheless, the MEAM predicts very low solubility of Si in Au (<1.3%) and Au in Si ($<10^{-6}$) in the solid phase, consistent with experimental measurements of <2% and $<2 \times 10^{-4}$ [37].

The last step is to fine-tune the potential by adjusting the parameter γ in the EOS function (for the B1 structure), and the cut-off parameters $C_{min}(i, j, k)$ in the multi-body screening function to fit the experimental binary phase diagram as closely as possible. Because the elastic constants of the B2 structure, one of the benchmarks for our potential model (see appendix B), are highly sensitive to $C_{min}(1, 1, 2)$ and $C_{min}(2, 2, 1)$, we use only γ, $C_{min}(1, 2, 1)$, and $C_{min}(1, 2, 2)$ when adjusting the free energy of the liquid alloy. Without any correction to γ, the free energy of mixing of liquid is too high and so is the eutectic temperature. As the binding energy of Au–Si is smaller than the average of the Au–Au and Si–Si binding energies, we increase γ to make the Au–Si cross-potential more repulsive, in order to reduce the free energy of mixing for liquid for the entire composition range. $C_{min}(1, 2, 1)$ and $C_{min}(1, 2, 2)$ are adjusted to change the multi-body screening effects selectively. Decreasing $C_{min}(1, 2, 1)$ (the factor of screening of Au–Si by Au) lowers the Au-rich part of liquid free energy because it reduces the effects of screening by Si atoms on Au–Au interactions. In the same way, we can increase $C_{min}(1, 2, 2)$ to raise the Si-rich part of the liquid free energy. We repeated these procedures until

Table 3. Parameters for the Au–Si MEAM cross-potential using B1 as the reference structure. $C_{\min}(i, j, k)$ are cut-off parameters in the multi-body screening function. They describe the effect on the interaction between atoms of type i and j of screening by their common neighbor of type k, where $i, j, k = 1$ (Au) or 2 (Si). The same $C_{\max}(i, j, k)$ is used for every combination of i, j, k.

E_c	r_e	α	$\frac{\rho_0^{Si}}{\rho_0^{Au}}$	$C_{\max}$
4.155	2.700	5.819	1.48	2.8
$C_{\min}(1, 1, 2)$	$C_{\min}(1, 2, 1)$	$C_{\min}(1, 2, 2)$	$C_{\min}(2, 2, 1)$	γ
1.9	0.95	1.85	1.0	0.26

we obtained a binary phase diagram and free energy of mixing close to the experimental ones. The resulting parameters for the MEAM Au–Si cross-potential are summarized in table 3.

The binary phase diagram of the resulting MEAM potential is shown in figure 1, together with the experimental phase diagram. The MEAM potential successfully captures the eutectic behavior. The eutectic temperature ($T_e = 629$ K) matches well with the experimental value (634 K). The eutectic composition ($x_e = 0.234$) also agrees well with the experimental value (0.195). The boundary of the Au-rich solid phase is not shown in the experimental phase diagram [37], but it is known that the maximum solubility of Si in Au is less than 2%, which is consistent with our value of 1.3%. We are not able to remove the slight offset of the liquidus curve for the Au-rich branch. This seems to be a limitation of the functional form of the MEAM potential used in this work. Additional benchmark data for the potential are presented in appendix B. The method used for computing the binary phase diagram for a given interatomic potential model is presented in section 3.

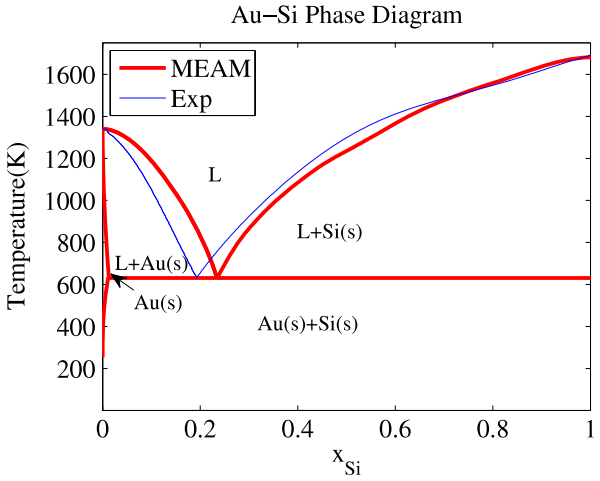

Figure 1. The binary phase diagram of Au–Si. The MEAM prediction is plotted as a thick line and the experimental phase diagram is plotted as a thin line. L corresponds to the liquid phase. Au(s) and Si(s) correspond to the Au-rich and Si-rich solid phases, respectively.

3. Construction of the binary phase diagram

To compute the Au–Si binary phase diagram, we need the Gibbs free energy (per atom) as a function of temperature T and composition $x = x_{Si}$ for three phases: (1) FCC Au crystal with Si impurities G_{FCC}, (2) DC Si crystal with Au impurities G_{DC}, and (3) liquid Au–Si alloy G_{liq}. At a given temperature, the range of stability on the composition axis for each phase and their mixtures is determined by the common tangent construction.

The free energy at a given temperature is obtained by the adiabatic switching method [32], which computes the free energy difference between the system and a reference whose free energy is known analytically. The change of free energy as a function of temperature is then computed using the reversible scaling method [33]. We have used these methods to compute the free energy of single-component systems (in both solid and liquid phases) and determined their melting points [34]. In the following, we will focus on the extra complexities caused by the binary systems, such as the configurational entropy.

3.1. Free energy of a solid with impurities

The solid free energies of pure Au (FCC) and pure Si (DC) can be computed using the method described earlier [34]. These correspond to $G_{FCC}(x = 0, T)$ and $G_{DC}(x = 1, T)$, respectively. In the calculation of G_{FCC} and G_{DC} as a function of x, we notice that the solubility in the solid phase for both Si in Au and Au in Si is very low. This means that we only need to know $G_{FCC}(x, T)$ in the vicinity of $x = 0$. Similarly, we only need to know $G_{DC}(x, T)$ in the vicinity of $x = 1$. In the following, we describe our approach for obtaining $G_{FCC}(x, T)$. $G_{DC}(x, T)$ can be obtained in a similar way.

For an FCC Au crystal containing a very low concentration of Si impurities ($x \ll 1$), it is reasonable to assume that the impurities are not interacting with each other. In this limit, the free energy per atom of the crystal can be approximated by [35]

$$G_{FCC}(x, T) \approx G_{FCC}(x = 0, T) + x\,\Delta g_{imp}(T) - T s_{mix}(x) \quad (4)$$

where Δg_{imp} is the free energy of a single impurity, in which the configurational entropy is ignored, i.e. only the vibrational entropy is included. $s_{mix} = -k_B[x \ln x + (1 - x)\ln(1 - x)]$ is the configurational entropy of mixing.

We compute Δg_{imp} in equation (4) using a simulation cell containing $N - 1 = 499$ Au atoms and one Si atom under periodic boundary conditions (PBC). We label this simulation cell as Cell 1 and let G^1 be its free energy. G^1 at a given temperature ($T_0 = 254$ K) is[3] computed by adiabatically switching [32] the system to its harmonic approximation, whose free energy is known analytically [34]. G^1 as a function of temperature is then computed by the reversible scaling method [33]. Similarly, we compute the free energy G^0 as a function of temperature, for a simulation cell containing 500 Au atoms. The free energy of the impurity is simply

$$\Delta g_{imp}(T) = G^1(T) - G^0(T) + k_B T \ln N. \quad (5)$$

The $k_B T \ln N$ term is added to cancel the configurational entropy contribution in $G^1(T)$.[4] Figure 5(a) plots $G_{FCC}(x, T)$

[3] To improve accuracy, we also performed an independent calculation at $T_0 = 629$ K.

[4] The configurational entropy of mixing in Cell 1 is $S^1_{mix} = k_B \ln \frac{N!}{(N-1)!1!} = k_B \ln N$.

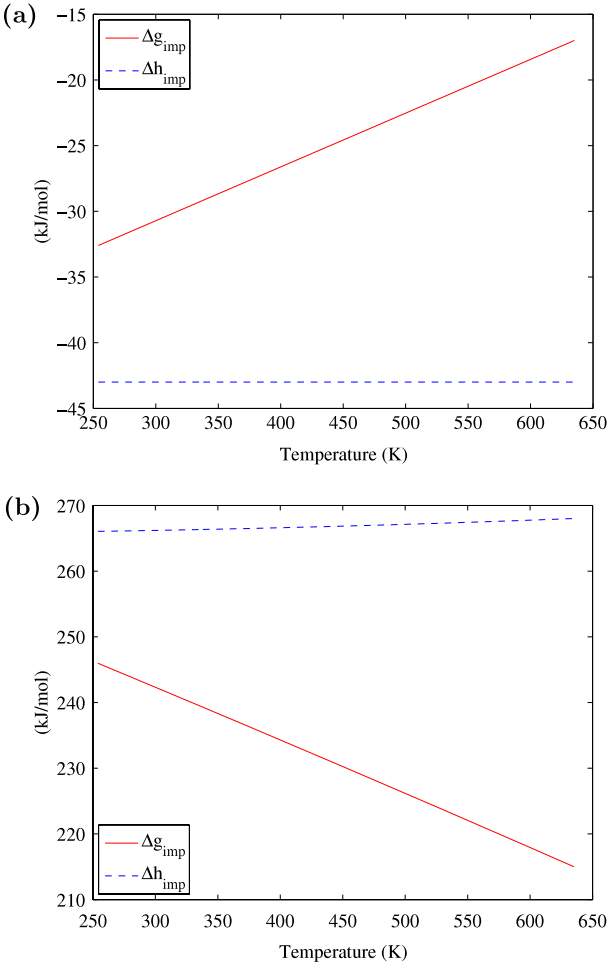

Figure 2. The Gibbs free energy $\Delta g_{\rm imp}(T)$ and enthalpy $\Delta h_{\rm imp}(T)$. (a) A Si impurity within a Au crystal. (b) A Au impurity within a Si crystal.

and $G_{\rm DC}(x, T)$ as a function of x at $T = 700$ K, obtained using the method described above.

In several studies regarding binary phase diagram calculations [23, 24], it is common to approximate $\Delta g_{\rm imp}(T) = \Delta h_{\rm imp} - T\,\Delta S_{\rm vib}$ by the enthalpy $\Delta h_{\rm imp}$, neglecting the vibrational entropy contribution in $\Delta g_{\rm imp}(T)$. However, we find that the contribution from $-T\,\Delta S_{\rm vib}$ is significant for the Au–Si system, affecting the phase diagram significantly. Figure 2 plots $\Delta g_{\rm imp}(T)$ and $\Delta h_{\rm imp}(T)$ as a function of temperature. On one hand, the vibrational entropy change for the Si impurity inside the Au crystal is $-4.9k_{\rm B}$, which increases the free energy by 26 kJ mol^{-1} at the eutectic temperature. The Si impurity solubility will be significantly overestimated if we ignore the vibrational entropy. On the other hand, for the Si impurity inside the Au crystal, $\Delta S_{\rm vib}$ is $10k_{\rm B}$, corresponding to a free energy decrease of 53 kJ mol^{-1} at the eutectic temperature. The sign of $\Delta S_{\rm vib}$ is opposite on each side, because the Si–Si bonding is stiffer than the Au–Au bonding. (The Debye temperature of Si is 645 K while that of Au is 165 K [39].) This result emphasizes the importance of including the vibrational entropy change in computing the free energy of the solid and the phase diagram.

3.2. Free energy of the liquid alloy

We first compute the Helmholtz free energy difference between the liquid alloy and the ideal gas at a given temperature using the adiabatic switching method[5]. To improve computational efficiency, a fluid with a purely repulsive (Gaussian) potential is used as an intermediate reference system during the switching [34]. To obtain the free energy of the liquid alloy at this temperature, we add this free energy difference to the free energy of the two-component ideal gas under a fixed center-of-mass constraint, which is [36]

$$F_{\rm i.g.}(N_1, N_2) = -N_1 k_{\rm B}T \ln\frac{V}{\Lambda_1^3} - N_2 k_{\rm B}T \ln\frac{V}{\Lambda_2^3} + k_{\rm B}T \ln\frac{V}{\Lambda_{\rm e}^3} + k_{\rm B}T \ln(N_1!N_2!) \quad (6)$$

where V is the volume of the simulation cell, $\Lambda_i = h/\sqrt{2\pi m_i k_{\rm B}T}$ is the de Broglie wavelength, with $i = 1$ for Au and $i = 2$ for Si. $\Lambda_{\rm e} = h/\sqrt{2\pi m_{\rm e} k_{\rm B}T}$ and $m_{\rm e} = (N_1 m_1^2 + N_2 m_2^2)/(N_1 m_1 + N_2 m_2)$ is the effective mass for the constrained degree of freedom. The last term in equation (6) reflects the configurational entropy of mixing. Once the free energy at a certain temperature is determined, its temperature dependence is obtained by reversible scaling [34].

Using the method above, we compute the free energy of the liquid alloy at 11 different compositions, $x = 0, 0.1, 0.2, \ldots, 1$, and interpolate the values along the x axis by spline fitting. The numerical error introduced in the spline fitting may have caused the undulation of the liquidus curve in the Si-rich region of the phase diagram in figure 1. Figure 3(a) plots the resulting function $G_{\rm liq}(x, T)$ at $T = 1250$ K. The difference between $G_{\rm liq}(x, T)$ and the straight line connecting the free energies of pure Au and pure Si liquids is the free energy of mixing, which is shown in figure 3(b). The prediction of the free energy from the MEAM model is in reasonable agreement with the CALPHAD result [38].

We also compare our model directly to the enthalpy of mixing and excess free energy from experiments [40], which are obtained by calorimetric and Knudsen cell methods respectively, as shown in figure 4. While qualitative agreements can be observed among MEAM, CALPHAD and experimental data, notable discrepancies can also be observed, even though the binary phase diagrams predicted by MEAM and CALPHAD both agree very well with the experimental phase diagram. This is because the MEAM potentials for pure Au and pure Si have ∼15% error in the latent heat (see appendix A). Therefore, the free energy differences between solid and liquid phases in the limits of $x = 0$ and 1 are incorrectly predicted by MEAM at low temperatures. To reproduce the experimental phase diagram, the shape of the liquid free energy curve as a function of x predicted by MEAM must be different from that predicted by CALPHAD at low temperatures. To remove this discrepancy, one will have to re-fit the MEAM potential for pure Au and pure Si to obtain the latent heat exactly.

[5] Because the liquid alloy is at zero pressure, its Gibbs free energy coincides with its Helmholtz free energy, although this is not the case for the reference ideal gas system.

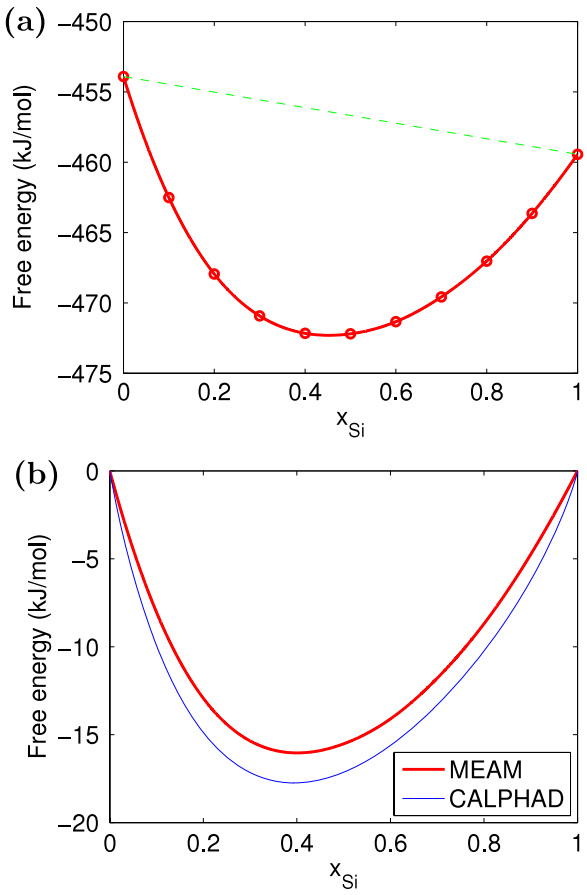

Figure 3. (a) The liquid free energy $G_{\rm liq}(x, T)$ at $T = 1250$ K. Circles are simulation results, which are fitted to a spline (solid line). A straight line connecting the liquid free energy of pure Au and pure Si is drawn for comparison. (b) The free energy of mixing $G_{\rm mix}(x, T)$ for the liquid phase at $T = 1250$ K. The predictions from the MEAM potential is plotted as a thick line, which is the difference between $G_{\rm liq}(x, T)$ and the straight line shown in (a). The free energy obtained from the CALPHAD method [38] is plotted as a thin line.

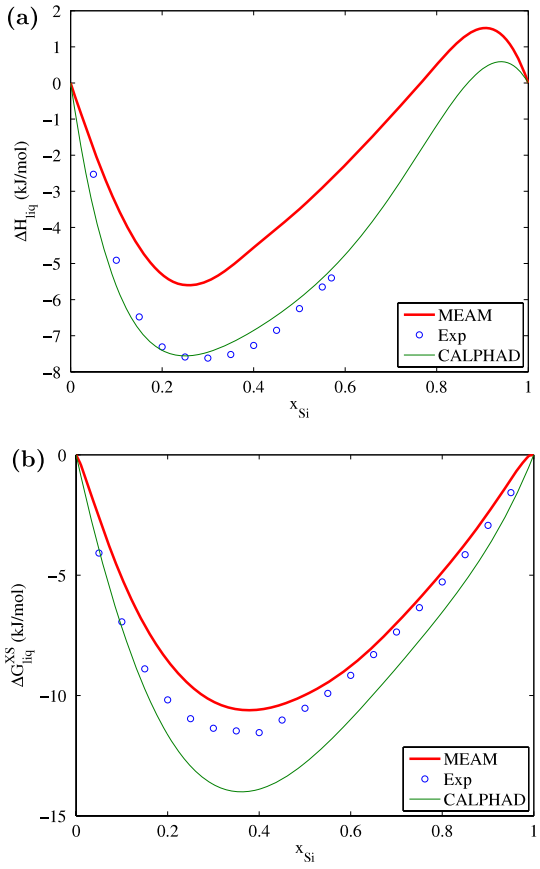

Figure 4. (a) The enthalpy of mixing $\Delta H_{\rm liq}(x, T)$ at $T = 1373$ K from experiments (circles), MEAM (thick line), and CALPHAD (thin line). (b) The excess free energy of mixing $\Delta G^{\rm XS}_{\rm liq}(x, T)$ at $T = 1685$ K from experiments (circles), MEAM (thick line), and CALPHAD (thin line).

3.3. Construction of the binary phase diagram

Given the Gibbs free energies of the three phases, $G_{\rm FCC}(x, T)$, $G_{\rm DC}(x, T)$ and $G_{\rm liq}(x, T)$, the binary phase diagram is constructed by drawing common tangent lines between the three curves at each temperature. An example is given in figure 5 for $T = 700$ K.

First, a common tangent line is drawn between $G_{\rm FCC}(x, T)$ and $G_{\rm liq}(x, T)$. The tangent contacts the two free energy curves at $x_1 = 0.011$ and $x_2 = 0.225$, respectively. This means that the Au-rich FCC (solid) phase is stable in the composition range of $x \in [0, x_1]$. The mixture of FCC solid and liquid phase is stable in the composition range of $x \in (x_1, x_2)$.

Second, a common tangent line is drawn between $G_{\rm liq}(x, T)$ and $G_{\rm DC}(x, T)$. The tangent contacts the two free energy curves at $x_3 = 0.251$ and $x_4 \approx 1$, respectively. This means that the Si-rich DC (solid) phase is stable in the composition range of $x \in [x_4, 1]$. The mixture of DC solid and liquid phase is stable in the composition range of $x \in (x_3, x_4)$. The liquid phase is stable in the composition range of $x \in [x_2, x_3]$. Repeating this procedure for all temperatures allows us to construct the binary phase diagram shown in figure 5(b). At the eutectic temperature $T_{\rm e} = 629$ K, all three free energy curves share the same tangent line ($x_2 = x_3$).[6] The tangent line contacts the liquid free energy curve at the eutectic composition $x_{\rm e} = 0.234$. The eutectic temperature and composition of the MEAM model are in good agreement with the experimental data (634 K and 0.195).

4. Summary

We develop a MEAM gold–silicon potential that is fitted to the experimental binary phase diagram. The potential parameters are first fitted to *ab initio* data of a hypothetical B1 alloy structure. The parameters are then adjusted to fit the substitutional impurity energies in the solid phase and the binary phase diagram. The final potential successfully captures the eutectic behavior of the gold–silicon binary system. The eutectic temperature and composition agrees well with experimental values. The potential is further benchmarked for

[6] At $T < T_{\rm e}$, the liquid free energy curve is entirely above the common tangent line of the two solid free energy curves. In this case, the liquid phase is unstable at any composition.

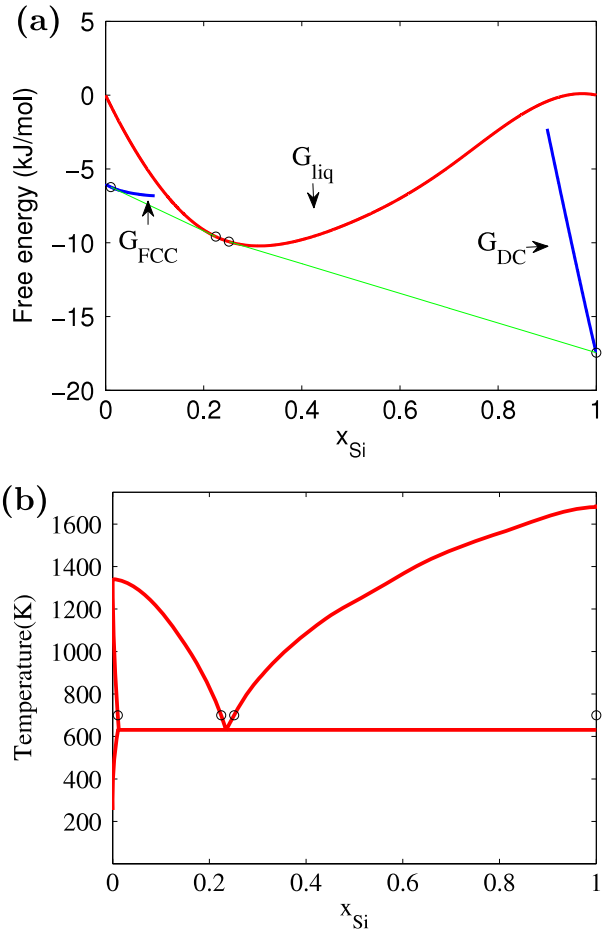

Figure 5. The common tangent method used to construct the binary phase diagram from free energy curves. (a) The Gibbs free energy of the three phases, $G_{\mathrm{FCC}}(x, T)$, $G_{\mathrm{DC}}(x, T)$ and $G_{\mathrm{liq}}(x, T)$, as a function of the composition x at $T = 700$ K. All of them are referenced to the free energies of pure Au liquid and pure Si liquid. Common tangent lines are drawn between $G_{\mathrm{FCC}}(x, T)$ and $G_{\mathrm{liq}}(x, T)$ (from $x_1 = 0.011$ to $x_2 = 0.225$), and between $G_{\mathrm{liq}}(x, T)$ and $G_{\mathrm{DC}}(x, T)$ (from $x_3 = 0.251$ to $x_4 \approx 1$). (b) The binary phase diagram of the MEAM Au–Si potential. The phase boundaries at $T = 700$ K are determined from the data in (a).

other hypothetical structures such as B2 and $L1_2$ in appendix B. The lattice constant, bulk modulus and cohesive energy are all within 15% of the *ab initio* results. We expect that the potential developed here could be used for atomistic simulations of gold-catalyzed nucleation and growth of silicon nanowires. Because this potential is mostly fitted to bulk properties, it can be further improved by fitting to surface and defect properties, which are also expected to influence the nanowire growth process. The method developed here for computing the binary phase diagram can also be used for other binary systems that exhibit a eutectic behavior and low solid solubility, such as the gold–germanium and gold–aluminum ones.

Acknowledgments

This work was partly supported by the DOE/SciDAC project on Quantum Simulation of Materials and Nanostructures and NSF/CMMI Nano Bio Materials Program CMS-0556032. SR acknowledges support from the Stanford Graduate Fellowship Program.

Appendix A. MEAM potentials for pure Au and pure Si

In the previous work [28], we improved the MEAM potentials for pure Au and pure Si. We used the second-nearest-neighbor MEAM model [41] for Au and the original MEAM model [14] for Si. Without modifying most of the parameters in the original models, we shift the melting points of pure Au and pure Si by adjusting the multi-body screening function through the C_{min} parameters and the pair potential function through the EOS function $E^u(r)$.

In determining the pair potential functions $\phi^{\mathrm{Au-Au}}(r)$ and $\phi^{\mathrm{Si-Si}}(r)$ of pure Au and pure Si, we use the following modification of the EOS function:

$$E^u(r) = -E_{\mathrm{c}}(1 + a^* + da^{*3} + \gamma a^{*4} \mathrm{e}^{-\lambda a^{*2}}/r)\ \exp(-a^*) \tag{A.1}$$

where $d = 0.05$, $\gamma = -0.182$ Å, $\lambda = 4.0$, and $C_{\mathrm{min}} = 0.8$ for pure Au, and $d = 0$, $\gamma = -0.36$ Å, $\lambda = 16.0$, and $C_{\mathrm{min}} = 1.85$ for pure Si. The new MEAM model of pure Au predicts the melting point $T_{\mathrm{m}} = 1337$ K and the latent heat $L = 14.2$ kJ mol^{-1}, which are closer to the experimental values of 1337.3 K and 12.6 kJ mol^{-1} than those predicted by the original MEAM model ($T_{\mathrm{m}} = 1120$ K and $L = 18.2$ kJ mol^{-1}). The new MEAM model of pure Si predicts $T_{\mathrm{m}} = 1687$ K and $L = 43.1$ kJ mol^{-1}, which are closer to the experimental values of 1685 K and 50.2 kJ mol^{-1} than those predicted by the original MEAM potential ($T_{\mathrm{m}} = 1411$ K and $L = 36.8$ kJ mol^{-1}). Notice that in this work, we use a different form of the EOS function to define the Au–Si pair potential, as given in equation (2).

Appendix B. Further benchmarks

We test the transferability of the Au–Si MEAM potential by comparing it against *ab initio* predictions on the energetics and elastic constants of several other hypothetical solid structures. Table B.1 presents the equilibrium lattice constants, cohesive energy, and elastic constants of B2 and $L1_2$ structures. The results for the B1 structure are also included. The values of a, B and E_{c} for the B1 structure are used in the fitting but the values of C_{11} and C_{44} are not. We intentionally fit the equilibrium lattice constant of the B1 structure to a higher value of $a = 5.400$ Å than the adjusted *ab initio* data (5.184 Å), to get better agreement with experiments on the binary phase diagram. A reasonable binary phase diagram can also be obtained by lowering the formation energy of the B1 structure instead, and using a large γ in equation (2). However, we do not take this approach because it changes the elastic constants of the B2 and $L1_2$ structures significantly. For all three phases, the MEAM predictions of a, B, E_{c}, and C_{11} are within 15% of *ab initio* data. Notice that the *ab initio* model predicts $C_{44} < 0$ for all three crystal structures, indicating that they are mechanically unstable. In comparison, the MEAM model predicts a small but positive C_{44}, meaning that they may be metastable in the MEAM model.

Table B.1. Comparison between MEAM and *ab initio* predictions for the energy and elastic properties of B1, B2 and $L1_2$ structures of Au–Si. a is the equilibrium lattice constant, B is the bulk modulus, E_c is the cohesive energy, and C_{11} and C_{44} are cubic elastic constants. The MEAM data should be compared with *ab initio* (DFT/LDA) results that have been adjusted for known differences from experimental values for pure elements.

Structure	Properties	DFT/LDA	DFT/LDA (adjusted)	MEAM
B1	a (Å)	5.161	5.184	5.400
	B (GPa)	129	127	127
	E_c (eV)	5.057	4.155	4.155
	C_{11} (GPa)	310	303	320
	C_{44} (GPa)	−20	−35	15
B2	a (Å)	3.202	3.226	3.370
	B (GPa)	130	128	114
	E_c (eV)	4.867	3.966	3.844
	C_{11} (GPa)	101	101	88
	C_{44} (GPa)	−3	−18	0.7
$L1_2$	a (Å)	4.041	4.055	4.192
	B (GPa)	156	152	140
	E_c (eV)	4.624	3.945	4.022
	C_{11} (GPa)	170	159	142
	C_{44} (GPa)	11	−1	19

References

[1] Lieber C M and Wang Z L 2007 *MRS Bull.* **32** 99
[2] Wong H-S P 2002 *IBM J. Res. Dev.* **46** 133
[3] Dubrovskii V G and Sibirev N V 2008 *Phys. Rev.* B **77** 035414
[4] Adhikari H, McIntyre P C, Marshall A F and Chidsey C E D 2007 *J. Appl. Phys.* **102** 094311
[5] Adhikari H, Marshall A F, Chidsey C E D and McIntyre P C 2006 *Nano Lett.* **6** 318
[6] Adhikari H 2008 *PhD Thesis* Stanford University
[7] Dubrovskii V G, Sibirev N V, Cirlin G E, Harmand J C and Ustinov V M 2006 *Phys. Rev.* E **73** 021603
[8] Schmidt V, Senz S and Gösele U 2007 *Phys. Rev.* B **75** 045335
[9] Daw M S and Baskes M I 1983 *Phys. Rev. Lett.* **50** 1285
[10] Stillinger F H and Weber T A 1985 *Phys. Rev.* B **31** 5262
[11] Tersoff J 1986 *Phys. Rev. Lett.* **56** 632
[12] Baskes M I 1987 *Phys. Rev. Lett.* **59** 2666
[13] Baskes M I, Nelson J S and Wright A F 1989 *Phys. Rev.* B **40** 6085
[14] Baskes M I 1992 *Phys. Rev.* B **46** 2727
[15] Lee B 2006 *Acta Mater.* **54** 701
[16] Lee B J, Wirth B D, Shim J H, Kwon J, Kwon S C and Hong J H 2005 *Phys. Rev.* B **71** 184205
[17] Kim Y and Lee B 2007 *Mater. Sci. Eng.* A **449** 733
[18] Cook S J and Clancy P 1993 *Phys. Rev.* B **47** 7686
[19] Zhang J M, Ma F and Xu K W 2004 *Appl. Surf. Sci.* **229** 34
[20] Grochola G, Russo S P, Yarovsky I and Snook I K 2004 *J. Chem. Phys.* **120** 3425
[21] Creemers C, Deurinck P, Helfensteyn S and Luyten J 2003 *Appl. Surf. Sci.* **219** 11
[22] Wang G F, Van Hove M A, Ross P N and Baskes M I 2005 *Prog. Surf. Sci.* **79** 28
[23] Caro A, Crowson D A and Caro M 2005 *Phys. Rev. Lett.* **95** 075702
[24] Pasianot R C and Malerba L 2007 *J. Nucl. Mater.* **360** 118
[25] Kuo C L and Clansy P 2004 *Surf. Sci.* **551** 39
[26] Kuo C L and Clansy P 2005 *J. Phys. Chem.* B **109** 13743
[27] Dongare A and Zhigilei L V 2005 *Proc. ICCES* p 2522
[28] Ryu S, Weinberger C R, Baskes M I and Cai W 2009 *Modell. Simul. Mater. Sci. Eng.* **17** 075008
[29] *The Vienna Ab Initio Simulation Package (VASP)* http://cms.mpi/univie.ac.at/vasp/
[30] Vanderbilt D 1990 *Phys. Rev.* B **41** 7892
[31] Rose J H, Smith J R, Guinea F and Ferrante J 1984 *Phys. Rev.* B **29** 2963
[32] Watanabe M and Reinhardt W P 1990 *Phys. Rev. Lett.* **65** 3301
[33] de Koning M, Antonelli A and Yip S 1999 *Phys. Rev. Lett.* **83** 3973
[34] Ryu S and Cai W 2008 *Modelling Simul. Mater. Sci. Eng.* **16** 085005
[35] Phillips R 2001 *Crystal, Defects and Microstructures: Modelling Across Scales* (Cambridge: Cambridge University Press)
[36] Ryckaert J P and Ciccotti G 1983 *J. Chem. Phys.* **78** 7368
[37] Okamoto H and Massalki H B 1983 *Bull. Alloy Phase Diag.* **4** 190
[38] Chevalier P-Y 1989 *Thermochim. Acta* **141** 217
[39] Kittel C 1996 *Introduction to Solid State Physics* 7th edn (New York: Wiley)
[40] Castanet R, Chastel R and Bergman C 1978 *Mater. Sci. Eng.* **32** 93
[41] Lee B J, Shim J H and Baskes M I 2003 *Phys. Rev.* B **68** 144112